Sensitivity of X-ray grating interferometry

P. Modregger,[1,2,*] B. R. Pinzer,[1] T. Thüring,[1,3] S. Rutishauser,[1] C. David,[4] and M. Stampanoni[1,3]

[1] *Swiss Light Source, Paul Scherrer Institut, Villigen, Switzerland*
[2] *University of Lausanne, School of Biology and Medicine, Lausanne, Switzerland*
[3] *Institute for Biomedical Engineering, UZH/ETH Zürich, Zürich, Switzerland*
[4] *Laboratory for Micro- and Nanotechnology, Paul Scherrer Institut, Villigen, Switzerland*

*peter.modregger@psi.ch

Abstract: It is known that the sensitivity of X-ray phase-contrast grating interferometry with regard to electron density variations present in the sample is related to the minimum detectable refraction angle. In this article a numerical framework is developed that allows for a realistic and quantitative determination of the sensitivity. The framework is validated by comparisons with experimental results and then used for the quantification of several influences on the sensitivity, such as spatial coherence or the number of phase step images. In particular, we identify the ideal inter-grating distance with respect to the highest sensitivity for parallel beam geometry. This knowledge will help to optimize existing synchrotron-based grating interferometry setups.

OCIS codes: (340.7440) X-ray imaging; (110.2990) Image formation theory; (110.3010) Image reconstruction techniques.

References and links

1. U. Bonse and M. Hart, "An X-ray interferometer," Appl. Phys. Lett. **6**, 155–156 (1965).
2. A. Momose, T. Takeda, Y. Itai, and K. Hirano, "Phase-contrast x-ray computed tomography for observing biological soft tissues," Nat. Med. **2**, 473–475 (1996).
3. A. Yoneyama, T. Takeda, Y. Tsuchiya, J. Wu, T.-T. Lwin, A. Koizumi, K. Hyodo, and Y. Itai, "A phase-contrast X-ray imaging system-with a 60 x 30 mm field of view based on a skew-symmetric two-crystal X-ray interferometer," Nucl. Instrum. Methods Phys. Res. A **523**, 217–222 (2004).
4. A. Snigirev, I. Snigireva, V. Kohn, S. Kuznetsov, and I. Schelokov, "On the possibilities of x-ray phase contrast microimaging by coherent high-energy synchrotron radiation," Rev. Sci. Instrum. **66**, 5486–5492 (1995).
5. P. Cloetens, R. Barrett, J. Baruchel, J.-P. Guigay, and M. Schlenker, "Phase objects in synchrotron radiation hard x-ray imaging," J. Phys. D: Appl. Phys. **29**, 133–146 (1996).
6. M. Langer, P. Cloetens, J.-P. Guigay, and F. Peyrin, "Quantitative comparison of direct phase retrieval algorithms in in-line phase tomography," Med. Phys. **35** 4556–4566 (2008).
7. T. J. Davis, D. Gao, T. E. Gureyev, A. W. Stevenson, and S. W. Wilkins, "Phase-contrast imaging of weakly absorbing materials using hard X-rays," Nature **373**, 595–598 (1995).
8. D. Chapman, W. Thomlinson, R. E Johnston, D. Washburn, E. D. Pisano, N. Gmür, Z. Zhong, R. H. Menk, F. Arfelli, and D. Sayers, "Diffraction enhanced x-ray imaging," Phys. Med. Biol. **42**, 2015–2025 (1997).
9. P. C. Diemoz, P. Coan, C. Glaser, and A. Bravin, "Absorption, refraction and scattering in analyzer-based imaging: comparison of different algorithms," Opt. Express **18**, 3494–3509 (2010).
10. M. Stampanoni, G. Borchert, R. Abela, and P. Rüegsegger, "Bragg magnifier: A detector for submicrometer x-ray computer tomography," J. Appl. Phys. **92**, 7630–7635 (2002).
11. P. Modregger, D. Lübbert, P. Schäfer, and R. Köhler, "Two dimensional diffraction enhanced imaging algorithm," Appl. Phys. Lett. **90**, 193501 (2007).

12. C. David, B. Nöhammer, H. H Solak, and E. Ziegler, "Differential x-ray phase contrast imaging using a shearing interferometer," Appl. Phys. Lett. **81** 3287–3289 (2002).

13. A. Momose, S. Kawamoto, I. Koyama, Y. Hamaishi, K. Takai, and Y. Suzuki, "Demonstration of X-Ray Talbot interferometry," Jpn. J. Appl. Phys. **42**, L866–L868 (2003).

14. T. Weitkamp, A. Diaz, C. David, F. Pfeiffer, M. Stampanoni, P. Cloetens, and E. Ziegler, "X-ray phase imaging with a grating interferometer," Opt. Express **13**, 6296–6304 (2005).

15. F. Pfeiffer, O. Bunk, C. David, M. Bech, G. Le Duc, A. Bravin, and P. Cloetens, "High-resolution brain tumor visualization using three-dimensional x-ray phase contrast tomography," Phys. Med. Biol. **52**, 6923–6930 (2007).

16. Z. Qi, J. Zambelli, N. Bevins and G.-H. Chen, "Quantitative imaging of electron density and effective atomic number using phase contrast CT," Phys. Med. Biol. **55**, 2669–2677 (2010).

17. F. Pfeiffer, O. Bunk, C. Schulze-Briese, A. Diaz, T. Weitkamp, C. David, J. F. van der Veen, I. Vartanyants, and I. K. Robinson, "Shearing interferometer for quantifying the coherence of hard X-ray beams," Phys. Rev. Lett. **94**, 164801 (2005).

18. Z.-T. Wang, K.-J. Kang, Z.-F. Huang, and Z.-Q. Chen, "Quantitative grating-based x-ray dark-field computed tomography," Appl. Phys. Lett. **95**, 094105 (2009).

19. M. Engelhardt, J. Baumann, M. Schuster, C. Kottler, F. Pfeiffer, O. Bunk, and C. David, "High-resolution differential phase contrast imaging using a magnifying projection geometry with a microfocus x-ray source," Appl. Phys. Lett. **90**, 224101 (2007).

20. M. Engelhardt, C. Kottler, O. Bunk, C. David, C. G. Schroer, J. Baumann, M. Schuster, and F. Pfeiffer, "The fractional Talbot effect in differential x-ray phase-contrast imaging for extended and polychromatic x-ray sources," J. Microscopy **232**, 145–157 (2008).

21. F. Pfeiffer, T. Weitkamp, O. Bunk, and C. David, "Phase retrieval and differential phase-contrast imaging with low-brilliance X-ray sources," Nat. Phys. **2**, 258–261 (2006).

22. T. Donath, M. Chabior, F. Pfeiffer, O. Bunk, E. Reznikova, J. Mohr, E. Hempel, S. Popescu, M. Hoheisel, M. Schuster, J. Baumann, and C. David, "Inverse geometry for grating-based x-ray phase-contrast imaging," J. Appl. Phys. **106**, 054703 (2009).

23. C. David, J. Bruder, T. Rohbeck, C. Grünzweig, C. Kottler, A. Diaz, O. Bunk, and F. Pfeiffer, "Fabrication of diffraction gratings for hard X-ray phase contrast imaging," Microelectron. Eng. **84**, 1172–1177 (2007).

24. E. Reznikova, J. Mohr, M. Boerner, V. Nazmov, and P.-J. Jakobs, "Soft X-ray lithography of high aspect ratio SU8 submicron structures," Microsyst. Technol. **14**, 1683–1688 (2008).

25. D. Noda, M. Tanaka, K. Shimada, W. Yashiro, A. Momose, and T. Hattori, "Fabrication of large area diffraction grating using LIGA process," Microsyst. Technol. **14**, 1311–11315 (2008).

26. H. F. Talbot, "Facts relating to optical science. No. IV," Philos. Mag. **9**, 401–407 (1836).

27. P. Cloetens, "Contribution to phase contrast imaging, reconstruction and tomography with hard synchrotron radiation: principles, implementation and applications," PhD thesis, Vrije Universiteit Brussel, 1999.

28. T. J. Suleski, "Generation of Lohmann images from binary-phase Talbot array illuminators," Appl. Opt. **36**, 4686–4691 (1997).

29. M. Stampanoni, A. Groso, A. Isenegger, G. Mikuljan, Q. Chen, D. Meister, M. Lange,, R. Betemps, S. Henein, and R. Abela, "TOMCAT: a beamline for tomographic microscopy and coherent radiology experiments," Synch. Rad. Instrum. **879**, 848-851 (2007).

30. S. A McDonald, F. Marone, C. Hintermüller, G. Mikuljan, C. David, F. Pfeiffer, and M. Stampanoni, "Advanced phase-contrast imaging using a grating interferometer," J. Synch. Rad. **16**, 562–572 (2009).

31. F. James, *Statistical Methods in Experimental Physics* 2nd ed. (World Scientific Publishing, 2006).

32. V. Revol, C. Kottler, R. Kaufmann, U. Straumann, and C. Urban, "Noise analysis of grating-based x-ray differential phase contrast imaging," Rev. Sci. Instrum. **81**, 073709 (2010)

33. A. Rack, T. Weitkamp, M. Riotte, D. Grigoriev, T. Rack, L. Helfen, T. Baumbach, R. Dietsch, T. Holz, M. Krämer, F. Siewert, M. Meduna, P. Cloetens, and E. Ziegler, "Comparative study of multilayers used in monochromators for synchrotron-based coherent hard X-ray imaging," J. Synch. Rad. **17**, 496–510 (2010).

34. T. Weitkamp, C. David, C. Kottler, O. Bunk, and F. Pfeiffer, "Tomography with grating interferometers at low-brilliance sources," Proc. SPIE **6318**, 63180S (2006).

35. R. Raupach and T. G. Flohr, "Analytical evaluation of the signal and noise propagation in x-ray differential phase-contrast computed tomography," Phys. Med. Biol. **56**, 2219–2244 (2011).

36. M. Bech, "X-ray imaging with a grating interferometer," PhD thesis, University of Copenhagen (2009).

37. T. Weitkamp, I. Zanette, C. David, J. Baruchel, M. Bech, P. Bernard, H. Deyhle, T. Donath, J. Kenntner, S. Lang, J. Mohr, B. Müller, F. Pfeiffer, E. Reznikova, S. Rutishauser, G. Schulz, A. Tapfer, and J.-P. Valade, "Recent developments in x-ray Talbot interferometry at ESRF-ID19," Proc. SPIE **7804**, 780406 (2010).

38. W. Yashiro, Y. Takeda, and A. Momose "Efficiency of capturing a phase image using cone-beam x-ray Talbot interferometry," J. Opt. Soc. Am. A **25**, 2025–2039 (2008).

1. Introduction

A wide variety of phase-sensitive X-ray imaging techniques have been suggested in recent years. For full-field imaging with parallel beam geometry several imaging methods may be distinguished: crystal interferometry [1–3], phase propagation imaging [4–6], analyzer-based imaging [7–11].

In addition, the grating interferometer (GI) is a recently established phase-sensitive X-ray imaging technique [12–14] that provides particularly high sensitivity to variations of the refractive index decrement within the sample [15], which is in turn proportional to the electron density present within the sample [16]. Typically, the GI utilizes a phase and an absorption grating in order to facilitate phase sensitivity. By applying a Fourier approach to data analysis it is possible to independently extract the contributions of absorption, differential phase contrast (DPC) and dark-field contrast [17, 18].

On the one hand, a major advantage offered by the GI is a low requirement for temporal beam coherence. It has been demonstrated that the GI is nearly achromatic [14], which opens the possibility to make use of a broad spectral width of the incident beam while preserving image quality. On the other hand, the requirements for spatial coherence (i.e. the angular source size at the position of the sample) are more demanding, but still allowing for an implementation of the GI at X-ray microfocus tubes [19, 20]. However, it has also been shown that imaging conditions at X-ray tubes with larger source sizes can be used by including an additional source grating into the experimental setup [21, 22].

For parallel beam geometry, spatial resolution of the GI is limited by either the pixel size of the detector or the pitch of the absorption grating [14] and, thus, by the manufacturing process. More generally speaking, the performance of the GI essentially depends on the quality of the gratings. Thus, considerable effort is put in the optimization of the production process [12, 23–25]. The challenge is to manufacture grating structures with particularly high aspect ratio in order to minimize residual transmission through the absorption grating. At the moment a pitch of a few microns is feasible leading to a moderate resolution in the same order of magnitude.

The aim of this article is to develop and establish a simple yet realistic model of noise for numerical simulations, whose applicability is not limited to the case of GI. This framework is then used for the theoretical estimation of the sensitivity of the GI in parallel beam geometry in terms of the minimum detectable refraction angle. As an application of this theoretical framework, the optimum inter-grating distance with respect to the sensitivity is determined. Finally, we show how this knowledge can be applied for the optimization of existing setups, which use synchrotron radiation.

2. Elements of the imaging process

The GI consists of a phase and an absorption grating downstream of the sample (see Fig. 1). It exploits Fresnel diffraction at periodic structures, which is related to the so-called Talbot effect [26, 27]. For the following itemization of well established facts parallel beam geometry is assumed. For cone beam geometry the appropriate adjustments apply [20], which are of negligible impact on the following discussion if the magnification is close to unity.

The phase grating introduces a periodic phase modulation into the incident wave, which then causes an observable periodic interference pattern at the so-called Lohmann distances [28]. For a phase shift of π, the period of the interference pattern equals half of the period of the phase grating g_1 and the Lohmann distances d_m are given by

$$d_m = \left(m - \frac{1}{2}\right)\frac{g_1{}^2}{4\lambda}, \quad \text{with} \quad m = 1, 2, \ldots \tag{1}$$

with λ the wavelength and m the diffraction order. Different equations hold true for phase
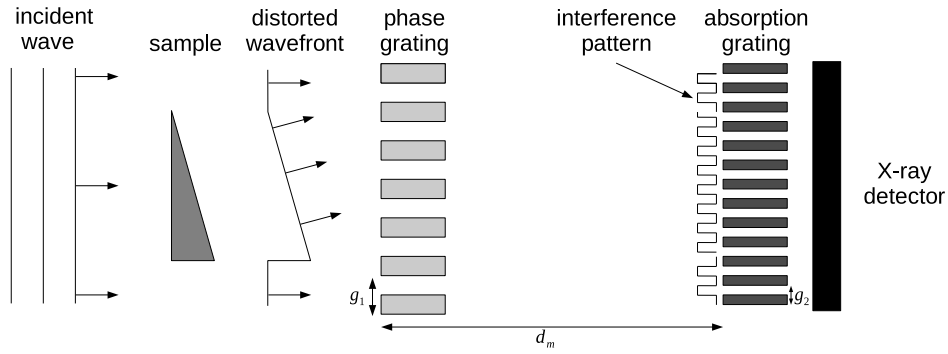
Fig. 1. Sketch of the grating interferometer. A phase grating and an absorption grating are exploited in order to provide phase-sensitivity.

gratings realizing a $\pi/2$, $2\pi/3$ or $4\pi/3$ phase shift [28].

The absorption grating is positioned at the desired Lohmann distance and acts as analyzer of the interference pattern. Its period matches the period of the interference pattern (i.e. $g_1 = 2g_2$). By laterally scanning either the phase grating or the absorption grating over one period of g_2, an intensity distribution for each pixel in the detector is acquired, which is referred to as the phase stepping curve (PSC; see Fig. 3).

In the experiment, a flat-field PSC $f(x)$ without the sample, where x denotes the lateral offset of the scanned grating, and a sample PSC $s(x)$ is obtained. Then the following Fourier component analysis [14,20] is applied to the PSCs in order to retrieve A, the absorption contrast

$$A = \hat{s}(q_0)/\hat{f}(q_0), \tag{2}$$

where the symbol "^" denotes the Fourier transform with respect to x and q_0 is the zeroth Fourier component, φ the lateral fringe offset

$$\varphi = \arg(\hat{s}(q_n)) - \arg(\hat{f}(q_n)), \tag{3}$$

where q_n denotes the n$^{\text{th}}$ harmonic Fourier component (corresponding to the number of periods measured) and B, the so-called dark-field contrast

$$B = \left| \left(\hat{s}(q_n)\hat{f}(q_0) \right) / \left(\hat{s}(q_0)\hat{f}(q_n) \right) \right|. \tag{4}$$

Usually, an additional baseline normalization is applied to determined the fringe offset value ϕ (i.e. subtracting the mean of ϕ over the field of view), in order to compensate for mechanical drift during acquisition. Using the small-angle approximation (i.e. $\tan \alpha \approx \alpha$) the lateral fringe offset φ is connected to the refraction angle α by

$$\varphi = 2\pi \frac{d_m \alpha}{g_2}. \tag{5}$$

However, if the lateral offset becomes larger than the period of the absorption grating, phase wrapping occurs. This means that φ values outside of $[-\pi, \pi]$ are falsely translated into this interval, which may be taken into account by including the appropriate modulus

$$\varphi = \mod\left(2\pi \frac{d_m \alpha}{g_2} + \pi, 2\pi \right) - \pi. \tag{6}$$

We like to point out that Eq. (6) will not be used for data analysis in this article.

In this context the values of φ are elements of the interval $[-\pi, \pi]$. According to Eq. (5) the contrast and, thus, the signal-to-noise ratio (SNR) of φ generally increases with the inter-grating distance d_m. But since phase wrapping as well as the finite spatial coherence are associated with loss of information, these effects essentially limit the accessibility of large inter-grating distances.

3. Experimental implementation at TOMCAT

The GI was integrated into the beamline for TOmographic Microscopy and Coherent rAdiology experimenTs (TOMCAT) of the Swiss Light Source [29] of the Paul Scherrer Institut (Villigen, Switzerland). The experimental implementation was performed focussing on fast data acquisition and post-processing and is now available to external users.

A 2.9 T bending magnet is used as the X-ray source providing a comparatively high photon flux at energies above 20 keV. In this energy range, the photon energy is selected by a W/Si double multilayer monochromator approximately 7 m from the source. The lines of the gratings are vertically oriented. The horizontal source size is around $125\,\mu$m (full width at half maximum) and the distance between source and phase grating amounts to 25 m.

The phase grating as well as the absorption grating (period: $2\,\mu$m) were manufactured in-house at the Laboratory for Micro- and Nanotechnology [23]. The x-ray beam is converted to visible light by a YAG:Ce scintillator of 250 μm thickness and subsequently imaged to a charged-coupled device (CCD). A pco.2000 (PCO AG, Kelheim, Germany) CCD camera is used for the detection of the optical photons. It offers a theoretical dynamic range of ≈ 12 bit with a pixel size of 7.4 μm. More details about the experimental implementation of grating interferometry at the TOMCAT beamline can be found in [30].

4. Sensitivity of the grating interferometer

The performance of the GI is closely related to the spatial coherence provided by the X-ray source. The goal of the following discussion is to identify the optimum inter-grating distance in terms of sensitivity for a predetermined set of experimental conditions (i.e. the source size S and the distance between source and phase grating z).

We will quantify the sensitivity of the GI in terms of the minimal detectable refraction angle α_{min}, which is proportional to the minimal detectable electron density variation in the sample. α_{min} corresponds directly to the signal-to-noise ratio (SNR) of radiographs and tomographic reconstructions. It was already experimentally demonstrated that refraction angles as small as $\alpha_{min} = 14$ nrad are accessible with the GI [15].

However, due to the Fourier nature of the data analysis algorithm (Eq. (3)) an approach to theoretically estimate α_{min} is not trivial. Thus, we propose a simple but reliable numerical procedure for the estimation of α_{min}.

It is well-known that the influence of a finite source size leads to a blurring of the interference pattern [34], which in turn will lead to a decreasing image quality. In order to quantify this effect in general terms, we introduce the reduced inter-grating distance η as

$$\eta = \frac{dS}{zg_2},\tag{7}$$

the dimensionless ratio between the projected source size Sd/z (d: inter-grating distance; z distance between source and phase grating) and the period of the interference pattern g_2.
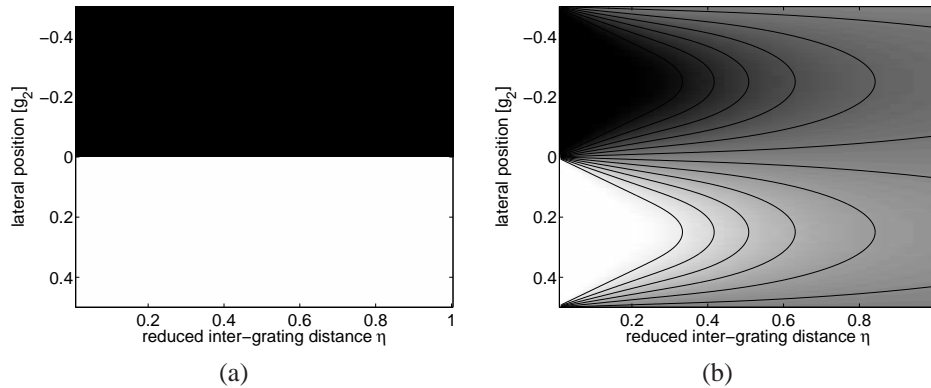
Fig. 2. (a) Ideal, rectangular-shaped interference pattern assumed for all inter-grating distances. (b) The interference pattern after convolution with the projected source distribution.

4.1. Numerical procedure

We have started with an ideal, rectangular-shaped interference pattern for all inter-grating distances d (Fig. 2(a)). Obviously, this does not represent an experimentally accessible situation and implies a different photon energy and/or diffraction order according to Eq. (1) for each inter-grating distance. However, this approach is appropriate for a general determination of the optimum inter-grating distance for a given combination of source size, source distance and pitch of the absorption grating g_2. In order to experimentally realize a given inter-grating distance, a phase grating has to be manufactured providing a phase shift of π at the determined photon energy.
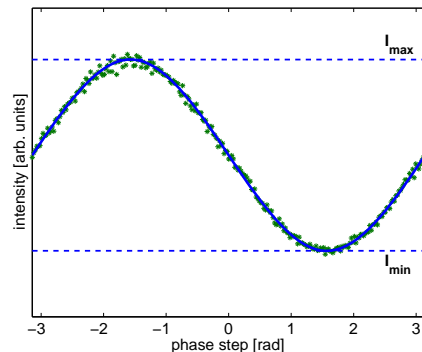

Fig. 3. Phase stepping curve and a representation of additional Gaussian noise, which is used in the numerical investigations. The calculations were performed with a reduced inter-grating distance of $\eta = 0.3$ (Eq. (7)).

In the second step, the influence of finite source size was included by the convolution of the projected source intensity distribution of Gaussian shape with the ideal interference pattern [20]. Figure 2(b) shows the blurred interference pattern as a function of η. The phase stepping curve (Fig. 3) was then calculated by a convolution of the interference pattern with the periodical, rectangular transmission function of the absorption grating.

Upon detection, the intensity at the detector is mapped to gray values I. For the reason of convenience we express gray values in terms of bit b with $I = 2^b$ throughout the article. In the

numerical simulations the maximum intensity I_{max} was set to a pre-defined value, which may reflect the experimental situation at hand or which may be taken as a free parameter. Gaussian noise with a mean of $\mu_n = I(x)$ and a standard deviation of $\sigma_n = \chi\sqrt{\mu_n}$ is added to the PSCs, where the factor χ will be discussed below. Then the Fourier component analysis (Eq. (3)) with $\arg(\hat{s}(q_n)) \equiv 0$ was applied to the resulting PSC yielding the fringe offset φ_k.

This was repeated for several thousand times and the standard deviation of the φ_k is taken as the uncertainty $\Delta\varphi$. For reliable distinction two φ-values must differ by more than $\Delta\varphi$ and, thus, the uncertainty $\Delta\varphi$ equals the minimum detectable fringe offset. According to Eq. (5) $\Delta\varphi$ directly relates to the minimum detectable refraction angle α_{min} by

$$\alpha_{min} = \frac{g_2}{2\pi d}\Delta\varphi. \tag{8}$$

The described numerical procedure delivers the minimum detectable refraction angle for a given set of parameters, such as the reduced inter-grating distance η or the number of phase steps M. By variation of the latter their impact on α_{min} can now be explored.

4.2. Modelization of noise

In the described model of the imaging process we assess that noise present in the experimental images essentially limits the accuracy of φ. Naturally, a realistic modelization of noise is essential to the viability of quantitative results with the procedure described in the previous subsection. Thus, we have established a simple yet realistic noise model that connects the noise used in the numerical simulations, to the noise present in the experiment.

For the numerical simulations we have chosen a Gaussian distribution of noise with μ_n the mean and σ_n the standard deviation [31]. However, μ_n and σ_n were not taken as independent parameters, but the relation

$$\chi = \frac{\sigma_n}{\sqrt{\mu_n}} \tag{9}$$

was used in order to determine σ_n of the noise distribution. Thus, we assess that the variance of the noise distribution (σ_n^2) increases linearly with the mean [32], which is justified by the linearity of the detector and the domination of photon shot noise (see further validation below). The factor χ takes into account the value mapping from number of photons to gray value during the process of detection. Thus, the χ value depends also on the gain of the detector and a gain larger than one results in χ values smaller than one [32].

In order to ensure a realistic modelization of noise, μ_n and χ were determined experimentally. For this purpose a series of 1000 flat-field images were taken at the position of maximum intensity of the PSC (see Fig. 3) at 25 keV with 121 mm inter-grating distance ($m = 2$ in Eq. (1)) and an exposure time of 450 ms. The following noise analysis was performed on a pixel basis, which means that all quantities were first determined for each pixel and with respect to the flat-field series . The values in the text represent the subsequently calculated mean and standard deviations over the field of view.

Figure 4(a) shows the pixel-wise mean gray value of the flat-field series. The average over the field of view was $\mu_n = (13.35 \pm 0.08)$ bit. While the horizontal stripes in the image are due to surface roughness of the monochromator [33], vertical stripes are caused by imperfections of the gratings. The factor χ (Eq. (9)) for each pixel is displayed in Fig. 4(b). An average of $\chi = 0.97 \pm 0.25$ was found. Here we point out that the exact value of μ_n has no influence on the described numerical procedure, since the results of the Fourier component analysis (Eqs. (2)–(4)) are invariant with respect to a scale factor of the PSCs. Only the ratio $\sqrt{\mu_n}/\chi$ is of interest, since it determines the noise level in the numerical simulations.

We emphasize that we use an effective model of noise, which takes almost all possible contributions of noise into account by fitting the parameters μ_n and χ to the experimental result.
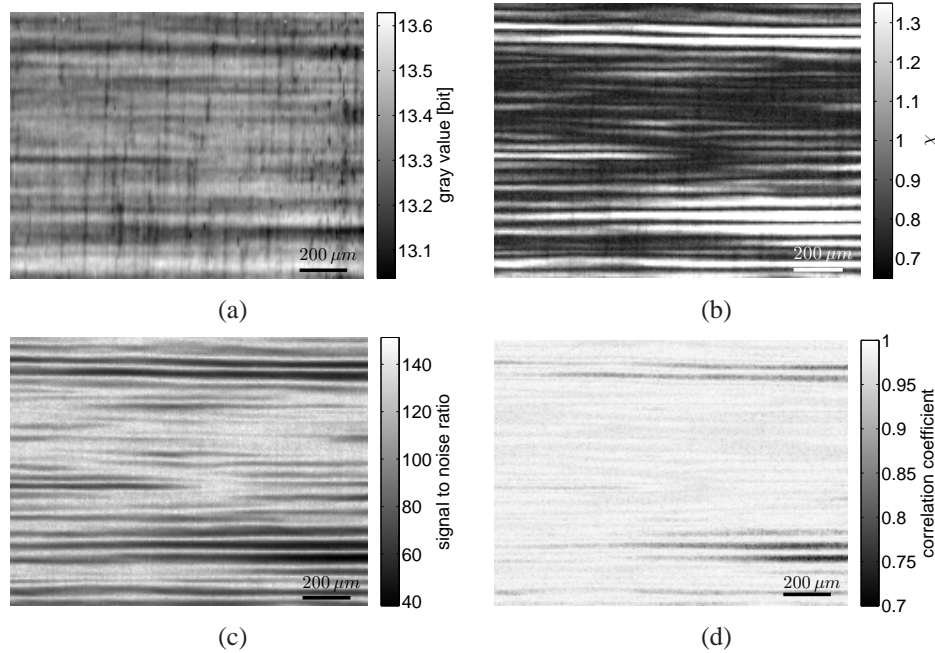
Fig. 4. For the determination of parameters and the validation of the noise model. (a) The mean of 1000 flat-field images acquired at the phase step of maximum intensity (ref. Fig. 3). While the horizontal stripes are due to surface roughness of the monochromator, the vertical stripes are caused by inhomogeneities. (b) Pixel-wise factor χ (see Eq. (9)). (c) The signal-to-noise ratio of the flat-field series (see Eq. (10)) over the field of view. Vibrations in the monochromator lead to a movement of the stripes between flat-field images. This increases the variance of gray values in the flat-field series for the affected pixel and, consequently, reduces the SNR. (d) Pixel-wise correlation coefficient between the theoretical prediction (see text) and the experimentally obtained gray value distribution in the flat-field series.

This is exemplified by the pixel-wise signal-to-noise ratio (SNR) with

$$SNR = \frac{\mu_n}{\sigma_n}, \tag{10}$$

of the flat-field series (Fig. 4(c)). Vibrations in the monochromator lead to a movement of the stripes between flat-field images. This increases the variance of gray values in the flat-field series and, consequently, reduces the SNR. Naturally, the distribution of this additional noise source is different from photon shot noise, which results into an increased χ for the affected pixels (Fig. 4(b)). However, the mean χ over the field of view is used in the numerical simulations and, thus, the monochromator vibrations are accounted for. A similar reasoning holds true for such additional noise sources as read-out or dark current noise. Due to the baseline normalization in the analysis procedure (see Sec. 2), effects of mechanical drift of the experimental setup are not taken into account.

We have validated the presented model of noise by using the determined parameter of the Gaussian noise (i.e. $\chi = 0.97$) for the prediction of the pixel-wise noise distribution of the flat-field series. For this purpose pixel-wise histograms were calculated with 50 bins (i.e. an average of 20 events per bin and pixel) around five times the standard deviation of the gray values distribution within the pixel. The histogram was then correlated with the predicted noise distribution and Fig. 4(d) shows the resulting correlation coefficient [31].

As might be expected, the correlation coefficient is comparably low in regions, which are most affected by beam fluctuations. However, the mean correlation coefficient over the field of view was 0.97 ± 0.03, which clearly validates the presented model of noise and its assumptions (e.g. Eq. (9)). Earlier, we have stated that the experimental noise is dominated by photon shot noise. Since the utilized Gaussian noise model represents the case of ideal photon shot noise, our statement is confirmed by the high correlation coefficient. Image areas of a reduced correlation coefficient (Fig. 4(d)) are due to local deviations in the noise distribution from the ideal Gaussian shape and maybe regarded as effects of the second order, which are caused by background fluctuations.

4.3. Results with constant η

The numerical simulations in this subsection were performed with parameters that reflect the typically experimental situation at TOMCAT (i.e. $\chi = 0.97$ and $\eta = 0.3$).
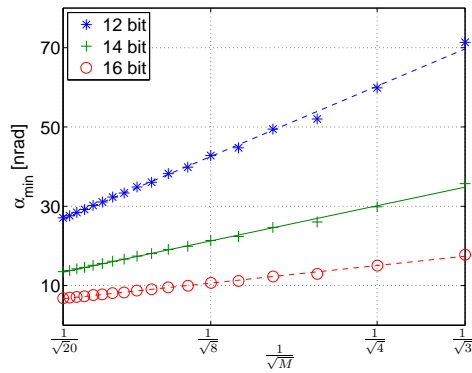

Fig. 5. Sensitivity of the GI as a function of $M^{-1/2}$ with M the number of phase steps for three different dynamic ranges, which are related to the noise level by Eq. (9). The lines indicate the results of linear regression.

First of all, we have investigated the effect of total number of phase steps M on the sensitivity α_{min}. Intuitive expectations suggest that α_{min} improves inversely with SNR if the exposure time for each phase step is constant: $\alpha_{min} \propto SNR^{-1}$. Poisson statistics then indicates that the SNR improves with the square root of the number of phase step images M: $SNR \propto M^{1/2}$. Thus, the sensitivity is expected to improve as $\alpha_{min} \propto M^{-1/2}$ and Fig. 5 shows that this expectation is met. The qualitative behavior is in total agreement with the published data [32, 38].

As a second example, the described procedure was used to determine the dependency of α_{min} on the visibility v, which is a characterization of the amplitude of the PSC. v is given by the ratio of the first and zeroth harmonic of the Fourier transform of the PSC

$$v = 2 \left| \frac{\hat{f}(q_1)}{\hat{f}(q_0)} \right|. \tag{11}$$

In addition to the blurring of the interference pattern caused by the finite source size, there are several potential sources degrading the visibility, e.g. insufficient attenuation of the absorption grating, polychromaticity of the X-ray beam, non-optimum manufacturing of the gratings or surface roughness of the monochromator. Instead of taking each individual effect into account, we use a variable transmission of the absorption grating to model the influence of decreased visibility.
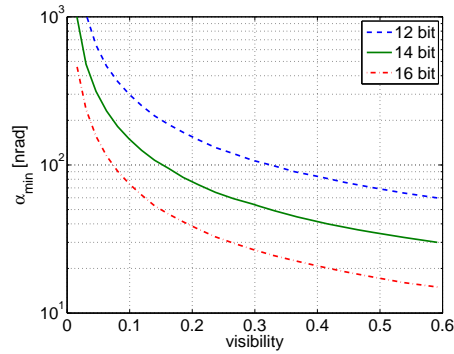
Fig. 6. Sensitivity of the GI in terms of the minimal detectable refraction angle as a function of the visibility for three different dynamic ranges, which are related to the noise level by Eq. (9).

The results (Fig. 6) show that sensitivity in the sub-μrad range is well accessible at TOMCAT. Furthermore, it is obvious that the visibility as well as the noise level have a dramatic impact on α_{min}.
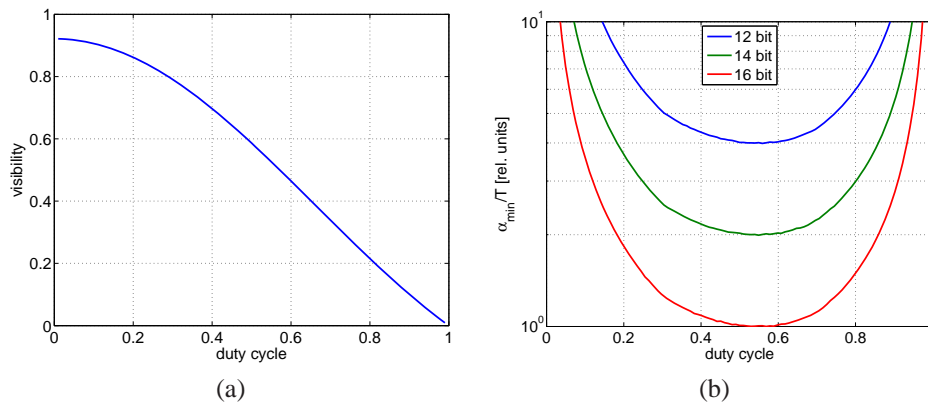

(a)

(b)

Fig. 7. Impact of the duty cycle of the absorption grating on the sensitivity or three different dynamic ranges, which are related to the noise level by Eq. (9). (a) Visibility (Eq. (11)) as a function of the duty cycle. (b) Minimum detectable refraction angle per time unit.

As an additional example, we have investigated the dependency of α_{min} on the duty cycle of the absorption grating. The duty cycle is defined as the ratio between the width of the transparent part of the grating structure and the pitch. Figure (7)a shows the visibility of the simulated PSCs according to Eq. (11) as a function of the duty cycle. Since a decreasing duty cycle is related to a finer sampling of the interference pattern, the visibility increases as the duty cycle decreases.

However, the larger visibility does not imply the superiority of smaller duty cycles. With increasing duty cycle the total number of acquired photons increases if the exposure time is constant. But the quantity of interest is the minimum detectable refraction angle per time unit. Thus, we have normalized the determined α_{min} by the duty cycle. The result is then the minimum detectable refraction angle per time unit (Fig. 7(b)). The optimum was found for a duty cycle of about 0.55.
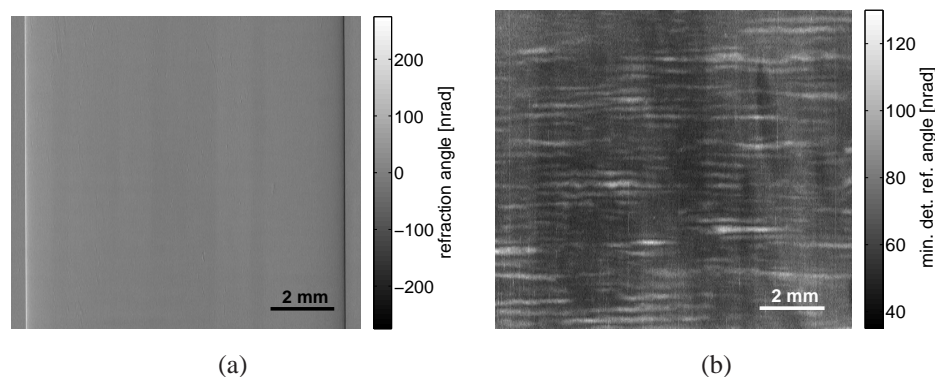
4.4. Comparison between theory and experiment

Fig. 8. For the experimental determination of the minimum detectable refraction angle. (a) The measured refraction angle of a polystyrene cylinder immersed in water. (b) The corresponding pixel-wise standard deviation of ten repeated scans, which is equal to the experimentally determined minimum detectable refraction angle.

Further validation of the presented numerical framework was performed by a comparison between theoretical prediction and experimental determination of the minimum detectable refraction angle. For the experiment a polystyrene (PS) cylinder of 10 mm diameter was immersed in water and scanned 100 times with the phase stepping procedure as described in Sec. 2. The number of phase steps was $M = 6$ over two PSC periods, the exposure time was 350 ms and the other experimental parameters were the same as in the previous section.

Figure 8(a) shows the resulting refraction angle. The contrast between water (refractive index decrement: $\delta = 3.68 \cdot 10^{-7}$) and PS ($\delta = 3.75 \cdot 10^{-7}$) is comparably low. The pixel-wise standard deviation of the 100 repeated scans (Fig. 8(b)) is taken as the minimum detectable refraction angle. The mean over the field of view is $\alpha_{min} = (67 \pm 9)$ nrad.

Up to now, we have assumed a perfect manufacturing of the gratings in the numerical simulations. Naturally, the experimental reality deviates from this ideal. In particular, the utilized phase grating has a non-ideal duty cycle of 0.59, which degrades the visibility of the PSCs. Thus, the visibility of the simulated PSC was lowered by increasing the parasitic transmission of the absorption grating (see also previous subsection) in order to match the visibility in experiment ($v = 0.2874$). Additionally, the effective dynamic range ($\mu_n = 13.06$) and, thus, implicitly the noise level in the numerical simulation was matched to the experimental situation.

The numerical determination of the minimum detectable refraction angle (see Sec. 4.1) yielded a theoretical prediction of $\alpha_{min} = 63$ nrad, which is in excellent agreement with the experimental result. Thus, we conclude that the presented framework makes accurate predictions.

The residual discrepancy may be explained by two influences that were not accounted for in the numerical framework. First, it was shown that the accuracy of the fringe offset φ depends on higher harmonics of the PSC and, thus, on the exact shape of the PSC [35]. As already mentioned, we assumed perfectly rectangular gratings in the simulations and deviations from this ideal case will act as an additional noise source. Secondly, the determination of the noise level (see Sec. 4.2) was performed on a single phase step position. Thus, effects of phase stepping jitter (i.e. an uncertainty of the position of the actuator used for the phase stepping) are not included into the noise. Both effects overestimate the sensitivity in the numerical framework. However, the agreement between simulations and experiment shows that these effects play a

minor role.

4.5. Optimum inter-grating distance

Finally, we have determined the optimum reduced inter-grating distance that maximizes the sensitivity for parallel beam geometry. Under otherwise optimal imaging conditions, two counteracting effects have to be taken into account.
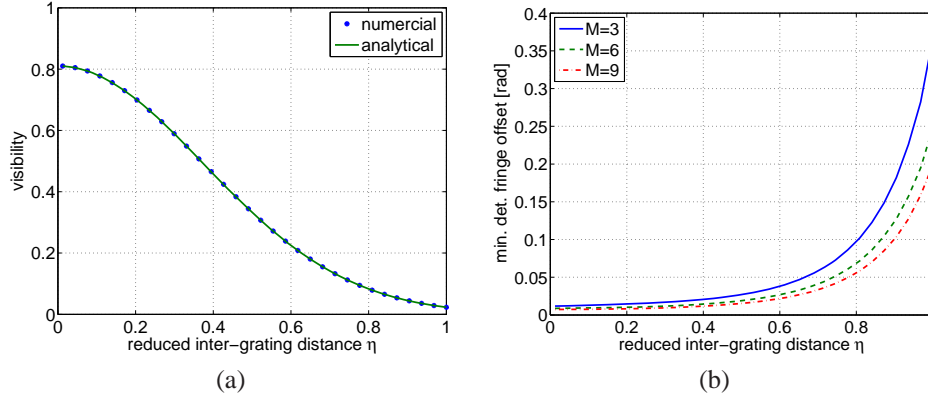

(a)   (b)

Fig. 9. (a) Visibility (Eq. (11)) in dependency on the reduced inter-grating distance η, which was numerically (see text) and analytically determined (Eq. (12)). (b) The corresponding uncertainty of the fringe offset $\Delta\varphi$ for three different dynamic ranges, which are related to the noise level by Eq. (9).
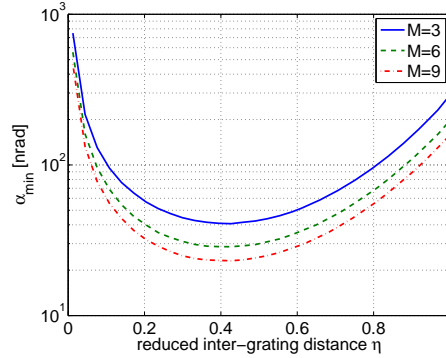

Fig. 10. Minimum detectable refraction angle α_{min} as a function of the reduced inter-grating distance η. M denotes the number of phase steps.

On the one hand, the finite source size increasingly blurs the interference pattern with increasing η (Fig. 2(b)), which results in a decreased visibility and, thus, into an increased minimum detectable refraction angle (Fig. 6). The first harmonic visibility v in dependency on the reduced inter-grating distance η is given by (see leading order term of Eq. (2.52) in [36])

$$v(\eta) = \frac{8}{\pi^2} e^{-(1.887\eta)^2}. \tag{12}$$

Figure 9(a) shows $v(\eta)$ as determined by Eq. (12) (unbroken green line) and as determined from the numerical calculations (dashed blue line). For the latter the PSCs were calculated

for any given η (see Sec. 4.1) and then analyzed with respect to Eq. (11). The corresponding minimum detectable fringe offset $\Delta\varphi$ was determined by the numerical procedure described in (see Sec. 4.1) corresponding the visibility in Fig. 9(a).

On the other hand, for a given refraction angle α the lateral shift of the interference pattern increases linearly with η, and, thus, the value of the fringe offset φ increases linearly along with the achieved contrast (Eq. (5)). Therefore, the contributions of increasing lateral fringe shift and decreasing visibility to the total sensitivity counteract each other and an optimal inter-grating distance maximizing the total sensitivity is expected.

The result of this investigation is presented in Fig. 10, where the optimum reduced inter-grating distance was identified as

$$\eta_{opt} = \frac{d_{opt}\,S}{z\,g_2} \approx 0.4. \tag{13}$$

While the quantitative values of α_{min} (i.e. the Y-axis) depend on the details of the experimental setup (e.g. detector, coherence or quality of the gratings), the optimum reduced inter-grating distance (i.e. the X-axis position of the minimum) does not depend on those details (ref. also to the results in [32, 35, 38]). Thus, measuring at $\eta = 0.4$ maximizes the sensitivity of all setups which employ a monochromatic, parallel beam geometry.

The identified optimum inter-grating distance is a prediction of the presented numerical framework, which is based on established facts (e.g. shape of the phase stepping curves, effects of coherence, etc.; see subsection 4.1) and an experimentally-confirmed noise model (subsection 4.2). Additionally, the numerical framework was validated for one point (subsection 4.4). Therefore, it seems unlikely that experimental reality substantially differs from this theoretical prediction.

5. Discussion

5.1. Optimization with existing gratings

Using the existing absorption grating at TOMCAT (i.e. $g_2 = 2\,\mu$m) the result $\eta = 0.4$ indicates an optimum inter-grating distance of $d_{opt} = 170$ mm with a minimum detectable refraction angle of $\alpha_{min} = 40$ nrad for 3 phase steps and ideal gratings. If a loss of 10% of sensitivity is assumed to be insignificant an interval of (120-230) mm may be considered as optimal.

Grating interferometry is also used at the ID19 beamline of the European Synchrotron Radiation Facility (Grenoble, France). At the ID19 the source distance is $z = 150$ m, the source size $S = 125\,\mu$m and absorption gratings with a pitch of $g_2 = 2.4\,\mu$m are employed [37]. According to Eq. (13) this implies an optimum inter-grating distance of 1.1 m.

Furthermore, the identified minimum detectable refraction angle for ideal gratings determines an upper bound limit for the resolution of the phase stepping motor. For the TOMCAT beamline the sensitivity of $\alpha_{min} = 40$ nrad at an optimum inter-grating distance of 170 mm corresponds to a lateral offset of the interference pattern of about 7 nm. Thus, the resolution and reproducibility of the corresponding motor has to be equal or better than 7 nm.

5.2. Optimum absorption grating

Up to now, we have treated the inter-grating distance d_m and the pitch of the absorption grating g_2 as independent parameters. However, for a given wavelength λ the two quantities are related by Eq. (1) if $g_1 = 2g_2$ holds (i.e. parallel beam). Therefore, the optimum reduced inter-grating distance determines the optimum pitch of the absorption grating by

$$\left(m - \frac{1}{2}\right) g_2 = \eta_{opt}\frac{z\lambda}{S} = \eta_{opt}L_{coh} \tag{14}$$

with L_{coh} the lateral coherence length. This result can now be used to optimize all existing GI setups, which employ a parallel beam geomtry.

Equation (14) indicates that for a given wavelength λ an optimum combination of m and g_2 exists. From the point of view of the manufacturing process, high aspect ratios of the absorbing grating lines are the current limitation [23]. The choice $m = 1$ would be ideal since it maximizes g_2, thus, significantly simplifying the process. At the same time $m = 1$ affects the flexible application of that particular absorption grating, since no smaller inter-grating distances can be realized. An absorption grating that is optimized for $m = 2$ can also be used for an $m = 1$ setup, which could avoid phase wrapping artifacts (see Eq. (6)) at the cost of non-optimal sensitivity. In practice, these advantages and disadvantages have to be weighed against each other.

5.3. Relation to published results

The quantification of the sensitivity of GI has been of increasing interest in the recent years. In the following, we relate the results of our investigation to the published data in works of Yashiro *et al.* [38], Revol *et al.* [32] and Raupach *et al.* [35].

Most closely related to the presented investigation is the article by Yashiro *et al.*. The authors identify the optimum experimental conditions for Talbot interferometry, which is a laboratory-based setup with cone beam geometry and two absorption gratings. In such a setup the source to detector distance R_2 becomes an additional parameter to optimize. Assuming a constant total beam intensity, the flux decreases with the square of R_2, which in turn leads to a decreased sensitivity for a fixed exposure time. This additional effect on the sensitivity is not applicable for parallel beam geometry, which was discussed here. In fact, the main difference between parallel and cone beam geometry with respect of optimizing the sensitivity is the occurrence of the factor $\eta_{opt} \approx 0.4$ in Eq. (14). Furthermore, in Yashiro *et al.* the sensitivity is numerically determined by Monte Carlo simulations with up to 10^{14} photons/sr per phase step image. Although the authors do not state the computation time, it is clear that our approach is much faster and easier to implement. As an example the computation time for Fig. 5 was about 6 min on a standard modern desktop computer.

Revol *et al.* derive analytical expressions for the sensitivity of the absorption, differential phase and dark-field contrast under the assumption of sinusoidal PSCs. While this assumption is valid for a laboratory-based setup with cone beam geometry, it does not hold true for the case of a synchrotron beamline. Due to the superior coherence the interference pattern is much closer to the ideal rectangular shape in the latter case. Thus, their results are not directly transferable to parallel beam geometry. While the modelization of noise and the method of experimental validation in Revol *et al.* was approximately similar to our investigations, they differ in the details. The analysis methods developed in Revol *et al.* assume a time-independent background illumination, which is obviously not valid for the present case (cf. Fig. 4). Furthermore, Revol *et al.* accounted for the additional noise source of phase stepping jitter, which we neglected. However, the authors reveal an interaction of sensitivities of the different contrasts. For example, the uncertainty of the fringe offset φ increases if the absorption or dark-field signal increases. In our investigations we implicitly assumed absent absorption and dark-field contrasts and we expect a similar behavior for parallel beam geometry.

The aim of the article of Raupach *et al.* is to compare the noise transfer from the experimental images to tomographic reconstruction for attenuation-based tomography and differential phase-contrast tomography (PCT). They discover a resolution-dependent performance ratio between the two techniques and identify a break-even point, which is given by the geometry and visibility of the PCT setup. The relevance of their investigation is the identification of the additional uncertainty of the fringe offset φ due to the higher harmonics in the PSC or - equivalently - the exact shape of the PSC. This effect (called "anatomical noise" in [35]) is taken into account

in our theoretical investigations, since all harmonics were present in the PSCs that were used as input for the numerical simulations. However, we assume ideal rectangular-shaped gratings and, thus, the corresponding ideally shaped PSCs in the numerical simulations, which explained the slight offset between theoretical prediction and experimental results in Sec. 4.4.

6. Conclusion

We have established a simple, fast yet reliable numerical procedure to quantify the sensitivity of grating interferometry in terms of the minimum detectable refraction angle. We presented and experimentally verified a noise model that accurately reflects major contributions of noise.

After confirming already published results concerning the dependency of the sensitivity on several experimental parameters, we investigated the dependency of the sensitivity on the duty cycle of the absorption grating. An optimum duty cycle of 0.55 was determined.

Further validation of the developed framework was performed by a comparison between theoretical prediction and experimental results. The latter were obtained with the GI setup at the TOMCAT beamline and for the specific experimental parameters a minimum detectable refraction angle of $\alpha_{min} = (67 \pm 9)$ nrad was identified, which was in excellent agreement with the theoretical prediction of $\alpha_{min} = 63$ nrad.

Furthermore, the numerical framework was used for the optimization of the sensitivity of GI in parallel beam geometry. We used the ratio of the period of the interference pattern and the projected source size η as a general parameter for describing the partial coherence contribution of finite source size. We identified the optimum reduced inter-grating distance, which maximizes the sensitivity, as $\eta_{opt} \approx 0.4$ for any beamline (see Eq. (13)).